Band gap and electron transport in epitaxial cubic $Cr_{1-x}Al_xN$(001)

Mary E. McGahay, Baiwei Wang ●, Jian Shi, and Daniel Gall ●

Department of Materials Science and Engineering, Rensselaer Polytechnic Institute, Troy, New York 12180, USA

A possible metal-insulator transition in the $Cr_{1-x}Al_xN$ alloy system is explored using electronic transport and optical measurements on epitaxial $Cr_{1-x}Al_xN$(001)/MgO(001) layers which form a cubic solid-solution rocksalt structure for $0 \leqslant x \leqslant 0.75$. The optical band gap E_g which is due to direct Γ-point transitions from the N-2p-like valence-band top to the majority spin e_g conduction-band minimum increases approximately linearly with Al content: $E_g = 0.64 + 2.81x$ eV. The room-temperature resistivity increases by a factor of 400, from $\rho = 0.070$ to $26 \, \Omega$ cm for $x = 0$–0.46, indicating an increasing carrier localization due to a decreasing Cr-Cr nearest-neighbor hybridization. However, ρ drops again to $< 0.38 \, \Omega$ cm for $x \geqslant 0.62$ which is attributed to midgap states that are also detected by optical absorption. Cooling to 77 K causes an increase in ρ by approximately one order of magnitude for all alloys ($x = 0$–0.75), suggesting that the decreasing localization length is compensated by an increasing density of states at the Fermi level. Oxygen exposure reduces the resistivity for $x \leqslant 0.46$ due to the formation of a conductive surface oxynitride, suggesting n-type doping by oxygen. X-ray-diffraction analyses including reciprocal-space maps indicate that the relaxed lattice constant decreases from $a_o = 0.4175$ to 0.4089 nm for $x = 0.0$ to 0.75, and that an increase to $x = 0.85$ leads to a breakdown of the cubic solid solution which is attributed to the nucleation of wurtzite-structure nanocrystals, causing also a steep increase in E_g and in the low-temperature resistivity due to enhanced carrier localization. The subgap refractive index at $h\nu = 0.5$ eV decreases from 4.8 for CrN to 3.1 for $Cr_{0.25}Al_{0.75}N$, due to the decreasing valence electron concentration. The overall results demonstrate that the quasibinary $Cr_{1-x}Al_xN$ system in the rocksalt structure retains the semiconducting properties of its parent binaries, cubic rocksalt structure CrN and AlN.

I. INTRODUCTION

$Cr_{1-x}Al_xN$ is a pseudobinary alloy which is based on cubic CrN [1–13] and is used as hard protective coating material [14,15] and also has potential for spintronic [16,17] or thermoelectric [18] applications. Its equilibrium crystal structure is (cubic) rocksalt for CrN-rich and (hexagonal) wurtzite for AlN-rich compositions, with a predicted cubic-to-hexagonal transition at $x = 0.772$ based on a structure map and two band parameters [19] or $x = 0.66$–0.815 based on first-principles thermodynamic calculations [20–22]. These predicted critical compositions are in agreement with thin-film deposition experiments which find a maximum AlN fraction in cubic rocksalt $Cr_{1-x}Al_xN$ of $x = 0.6$–0.75 [19,23–29]. Cubic $Cr_{1-x}Al_xN$ has a higher hardness and resistance to wear, oxidation, and corrosion than the binary CrN [23,26,27,29–33], and is particularly suitable for high-temperature applications because it does not undergo high-temperature spinodal decomposition [26,34,35], contrary to the related $Ti_{1-x}Al_xN$ alloy [34,36].

The electronic properties of $Cr_{1-x}Al_xN$ have been primarily explored in its wurtzite structure [19,25,27], which has less desirable mechanical properties [27,28] but has gained interest as a potential room-temperature dilute ferromagnetic semiconductor [16,17]. In contrast, relatively little is known about the electronic properties of cubic rocksalt $Cr_{1-x}Al_xN$. The pure binary CrN at room temperature exhibits disordered magnetic moments [2,6,8–10] and a narrow 0.2-eV band gap

[2,6,8,11,12] between the hybridized p-d valence and the d-conduction bands, and is referred to as a Mott-Hubbard [3,4,8,11,13] or a charge-transfer [2,5] insulator depending on if the valence-band top is considered to exhibit primarily d or p character, respectively [2,4–6,8,11,12]. Alloying CrN with AlN leads to changes in the electronic structure which are not *a priori* evident. The measured Seebeck coefficient transitions from negative for CrN(111) to positive for $Cr_{0.96}Al_{0.04}N$(111), indicating a transition from n- to p-type charge carriers and suggesting that Al in CrN acts as a p-type dopant [37]. This can be attributed to three vs six valence electrons in Al vs Cr but may also be affected by the composition in the samples of this study which are N rich [37]. In contrast, other studies on stoichiometric polycrystalline [38] and epitaxial [39,40] cubic rocksalt $Cr_{1-x}Al_xN$ layers report a resistance increase with the addition of Al and a negative temperature coefficient of resistivity (TCR) for the polycrystalline layers [38], suggesting that AlN acts as an alloying semiconductor rather than a dopant. With that interpretation, rocksalt $Cr_{1-x}Al_xN$ is a mixture of two semiconductors with indirect band gaps $E_g = 0.2$ eV [2,6,8,12] for CrN and $E_g = 4.0$–5.0 for AlN [41–47], where the latter values are theoretical predictions for AlN in the (unstable) rocksalt phase [42] while AlN in the equilibrium wurtzite structure has an $E_g = 6.11$ eV [22,48].

In this paper, we report the growth and electronic and optical properties of epitaxial cubic $Cr_{1-x}Al_xN$(001) layers deposited on MgO(001) by reactive cosputtering. X-ray-diffraction θ-2θ scans, ω rocking curves, and reciprocal-space

maps indicate that the layers are epitaxial and exhibit a single-phase solid-solution rocksalt structure without any detected secondary phases or misoriented grains for $x \leqslant 0.75$. The $Cr_{1-x}Al_xN(001)$ layers have a negative temperature coefficient of resistivity and an onset for optical absorption that increases with x, indicating that the alloys are semiconductors with a band gap that is controlled by the composition x, providing potential for band-gap engineering in a cubic rocksalt structure nitride.

II. EXPERIMENTAL PROCEDURE

$Cr_{1-x}Al_xN(001)$ layers were deposited in a three-chamber ultrahigh-vacuum DC magnetron sputtering system with a base pressure of 10^{-9} Torr and *in situ* transport measurement capabilities, as described in Refs. [49] and [50]. Prior to deposition, single-side polished $10 \times 10 \times 0.5$-mm^3 MgO(001) wafers were cleaned with successive rinses in ultrasonic baths of trichloroethylene, acetone, isopropyl alcohol, and deionized water, inserted into the deposition system and thermally degassed in vacuum at $1000\,°C$ for 1 h. Subsequently, the substrate temperature was lowered to the deposition temperature of $750\,°C$ and a constant flux of 99.999% pure N_2 that was further purified with a MicroTorr purifier was leaked into the chamber to reach a processing gas pressure of 3 mTorr. 5-cm-diameter 99.95% pure Cr and Al targets at a distance of 10.5 cm from the substrate and at an angle of $45°$ were sputter cleaned with closed shutters prior to deposition. Samples with different Al to Cr ratios were deposited by varying the DC power $P_{Cr} = 64–350$ W and $P_{Al} = 150–500$ W applied to the Cr and Al targets, respectively, yielding a deposition rate of 14–26 nm/min, as determined from thickness measurements by x-ray reflectivity, onto the substrate which was continuously rotated at 60 rpm to increase thickness and composition uniformity. The deposition time was adjusted so that all films had a nominal thickness of 300 nm. A Sparc-le 20 pulse module was used to reverse the voltage applied to the Al target every 50 μs for 5 μs at 10% voltage amplitude to neutralize possible target surface charging caused by the formation of an insulating AlN surface layer.

After deposition, the samples were allowed to cool to room temperature (295 ± 1 K), followed by transport to an adjacent analysis chamber without breaking vacuum. Resistivity measurements were done using an *in situ* linear four-point probe with spring-loaded tips with 1-mm interprobe spacings, a Keithley 2182A nanovoltmeter, and a Keithley 6220 precision current source providing 1.00 μA. Additional resistivity measurements were also taken after sample removal from the deposition system, using an *ex situ* four-point probe in air at 295 K and with the sample and probes immersed in liquid nitrogen at 77 K.

The composition of the $Cr_{1-x}Al_xN(001)$ layers was determined by Rutherford backscattering spectroscopy (RBS) using 2-MeV ^{4}He$^+$ ions incident at an angle of $6°$ relative to the sample surface normal and a total scattering angle of $166.2°$ between incident beam and detector. The acquired spectra were analyzed using the SIMNRA software. The experimental uncertainty for the measured backscattered intensities from the Cr and Al atoms is 2%, resulting in an uncertainty of the compositional parameter x of ± 0.01. In contrast, the relatively

weak scattering cross section of the light N atoms causes a larger uncertainty in the measured N to metal ratio of 5%.

X-ray diffraction (XRD) θ-2θ scans, ω-rocking curves, and asymmetric high-resolution reciprocal-space maps (RSMs) were obtained with a PANanalytical X'Pert Pro diffractometer with a Cu Kα source. Symmetric θ-2θ scans were collected over a 2θ range of $20°–90°$ using the Bragg-Brentano geometry with a $0.5°$ divergent incident beam and a 0.04-rad Soller slit in front of a PixCEL solid-state line detector operated in receiving mode with an active length of 0.165 mm. ω-rocking curves were obtained using a hybrid mirror with a two-bounce two-crystal Ge(220) monochromator and a solid-state detector set at a constant 2θ angle corresponding to the $Cr_{1-x}Al_xN$ 002 reflection. The same monochromator was employed for asymmetric high-resolution reciprocal-space maps around the 113 reflections, using the line detector in scanning mode with all 255 channels open to allow for fast, high-resolution mapping with a small angle ($10°–14°$) between the sample surface and the diffracted beam to cause beam narrowing which increases the 2θ resolution.

Optical ultraviolet to visible to infrared (UV-vis-IR) spectra were collected in a Perkin-Elmer Lambda 950 photospectrometer over the wavelength range 176–3300 nm in 2-nm-steps. The transmittance T was measured at normal incidence and reflectance R at a $6°$ angle relative to the surface normal. The transmission spectra were corrected for diffuse scattering from the unpolished back side of the substrate as determined from transmission measurements of the substrate without deposited layers. The reflection spectra were calibrated using the measured R of a Al mirror. The optical constants of the MgO substrates were determined from T and R spectra from the uncoated substrate and were used for the optical analysis. However, the absorption within the substrate was found to be negligible over the relevant wavelength range.

The reflection spectra of all layers showed strong interference fringes due to reflections at the air-film and the film-substrate interfaces. The positions of these fringes at λ_i were used to determine the index of refraction $n(\lambda)$ using $2d = (2i - 1)\lambda_i/(2n)$ for maxima and $2d = i\lambda_i/n$ for minima, where d is the film thickness, i is the interference fringe number, and the phase shifts for reflection at the air-film and film-substrate interfaces are π and 0, respectively. The uncertainty in the obtained values for n is estimated to be $\pm 4\%$, accounting for both measurement and data analysis/fitting uncertainties. In contrast, the uncertainties in the measured transmission and reflection intensities are 10 and 27%, respectively. The latter uncertainty is relatively large due to the sensitivity of R to sample alignment and variations in the beam position and direction caused by the monochromator. The optical absorption coefficient α is determined from the measured T using $\alpha = \ln([(1 - r_1)(1 - r_2)]/T)/d$ [51], where $d = 300$ nm is the film thickness, $r_1 = (1 - n_{film})^2/(1 + n_{film})^2$ is the reflection from the film-air interface and $r_2 = (n_{film} - n_{MgO})^2/(n_{film} + n_{MgO})^2$ is the reflection from the film-substrate interface. This expression neglects multiple reflections and associated interference effects, leading to a wavelength-independent absolute uncertainty in α of 1.2–2.7×10^4 cm^{-1} which decreases with increasing x and corresponds to an average relative uncertainty that decreases

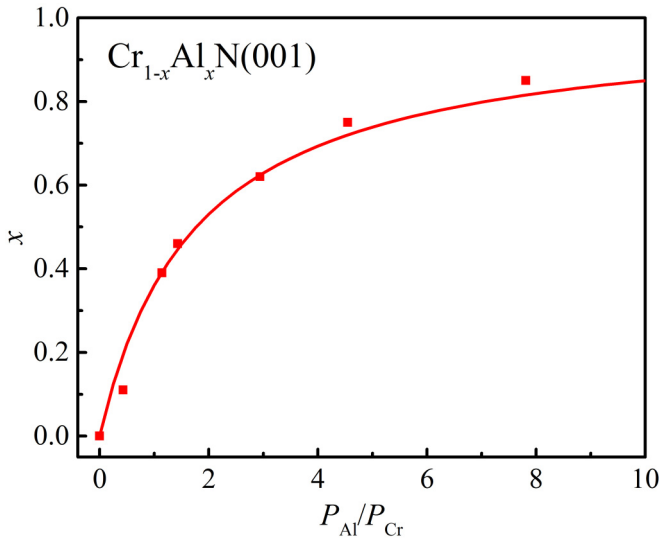FIG. 1. Al content x in $Cr_{1-x}Al_xN$ layers versus the ratio of power P_{Al}/P_{Cr} applied to the Al and Cr targets during deposition.

from 40% at small $\alpha = 5 \times 10^4 \, cm^{-1}$ to ~10% for $\alpha = 15 \times 10^4 \, cm^{-1}$.

III. RESULTS AND DISCUSSION

A. Structural properties

Figure 1 is a plot of the measured Al content x in the $Cr_{1-x}Al_xN(001)$ layers as a function of the power ratio P_{Al}/P_{Cr} applied to the Al and Cr targets during deposition. The data are obtained from the RBS analyses and indicate a monotonously increasing Al content $x = 0$–0.85 with increasing P_{Al}/P_{Cr}. The plot also includes a curve which is obtained from data fitting using the expression $x = (P_{Al}/P_{Cr})/(P_{Al}/P_{Cr} + C)$ which corresponds to the expected Al content under the assumption that the deposition rate of both materials increases linearly with power. The constant $C = 1.77$ is determined from curve fitting and corresponds to the power ratio at which $x = 0.5$. Thus, the deposition rate of Al is 1.77 times smaller than that of Cr for the same applied power. We attribute this to the combination of (i) a lower sputter rate of the insulating nitrided Al target surface in comparison to the more conductive nitrided Cr target surface and (ii) a 10% reduction in the effective Al deposition rate due to the pulsed-DC power applied to the Al target. The lower Al deposition rate is also in qualitative agreement with reports of a CrN deposition rate that is 2.66 [52] or 3.27 [53] times higher than that of AlN during pulsed closed-field unbalanced magnetron sputtering. The measured data are overall well described by the fitted curve but deviate slightly below and above the curve at low and high P_{Al}/P_{Cr}, respectively. This is exactly as expected, because deposition rates at low magnetron power tend to be below the linear trend that is assumed for the plotted curve.

The RBS analysis also provides values for the metal to nitrogen ratio in the layers, which was found to be 1.00 ± 0.05 for all samples, indicating a stoichiometric composition of the pseudobinary nitrides and justifying the use of "$Cr_{1-x}Al_xN$"

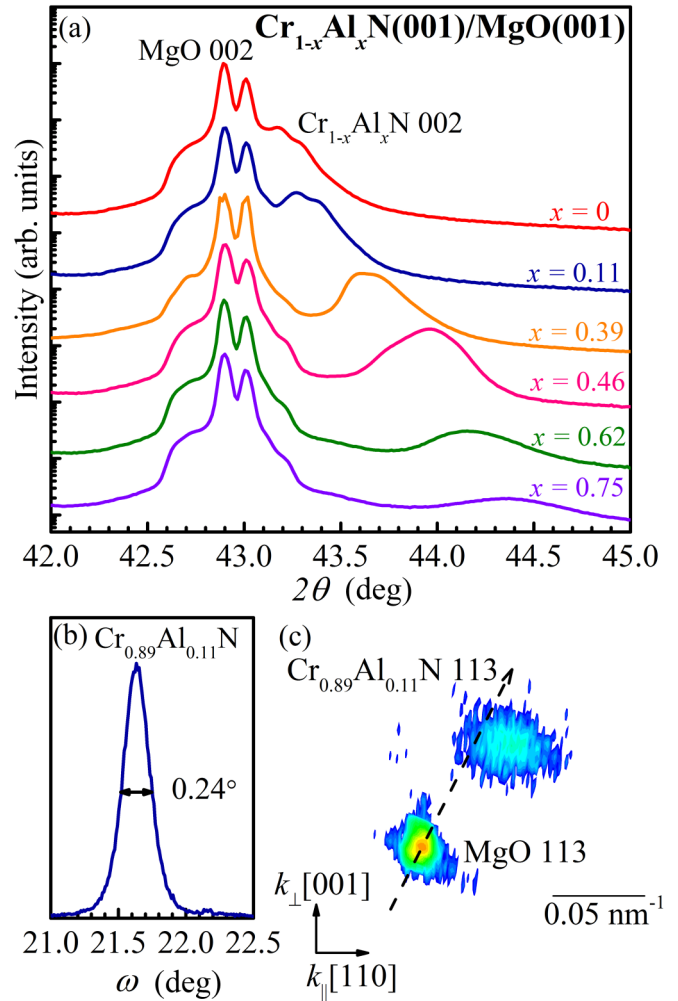FIG. 2. X-ray-diffraction (a) θ-2θ scans from epitaxial $Cr_{1-x}Al_xN(001)$ layers grown on MgO(001) with $x = 0$–0.75 and (b) ω-rocking curve of the 002 reflection and (c) reciprocal-space map of the 113 reflections from a $Cr_{0.89}Al_{0.11}N(001)$ layer.

for our layers throughout this paper. We note that this stoichiometric N to metal ratio is consistent with previous reports of epitaxial growth of CrN(001) deposited under comparable conditions but that substoichiometric (nitrogen-deficient) layers are expected for deposition above 700 °C [1,8,54,55].

Figure 2 shows sections of x-ray-diffraction θ-2θ patterns from $Cr_{1-x}Al_xN$ layers with $x = 0$–0.75. The measured intensities are plotted on a logarithmic scale and patterns from the different samples are shifted by an order of magnitude for clarity purposes. For all samples, the only peaks that could be detected in the measured 2θ range from 20° to 90° are within the plotted $2\theta = 42°$–$45°$ range, indicating a 001 orientation for all layers. The double-peak feature at 42.91° and 43.02° is evident in all patterns and is from the substrate MgO 002 reflections of the $Cu_{K\alpha1}$ and $Cu_{K\alpha2}$ x rays with wavelengths of 0.154 06 and 0.154 44 nm, respectively. The pattern from the pure CrN layer ($x = 0$) exhibits in addition a similar but 140 times less intense double peak at $2\theta = 43.19°$ and 43.30° which is from the CrN 002 reflections and indicates a CrN lattice constant in the growth direction $a_\perp = 0.4186$ nm. This value is slightly higher than the reported range of

0.4133–0.4185 nm for the bulk lattice constant of CrN [1,54,56], indicating compressive strain in our layer as quantified below and attributed to differential thermal contraction during cooling from the 750 °C growth temperature, similar to what has previously been reported for epitaxial CrN(001) grown on MgO(001) [1,54]. The alloy film with $x = 0.11$ yields peaks at $2\theta = 43.28°$ and $43.49°$. These peaks are associated with the 002 reflection from the $Cr_{0.89}Al_{0.11}N$ layer and have a similar intensity as for the pure CrN layer, but are shifted to the right which corresponds to a reduction in the lattice constant to $a_\perp = 0.4178$ nm. The corresponding peaks for the $x = 0.39$ pattern are at $2\theta = 43.64°$ and $43.74°$, yielding $a_\perp = 0.4145$ nm. These peaks are broader and 3 times less intense than for the pure CrN layer, indicating a reduced crystalline quality. This trend is continued as x is increased further to 0.46, 0.62, and 0.75, with peak intensities that are 3, 16, and 28 times lower than for $x = 0$. The alloy peaks also continue to shift to higher angles of $2\theta = 43.97°$, 44.17°, and 44.38°, yielding $a_\perp = 0.4118$, 0.4101, and 0. 4083 nm for $x = 0.46$, 0.62, and 0.75. These lattice constant values are determined using a weighted average x-ray wavelength of 0.154 18 nm, since the double-peak feature from $K_{\alpha 1}$ and $K_{\alpha 2}$ lines cannot be resolved for $x \geqslant 0.46$. The shoulders to the left and right of the substrate peaks are detected for all samples and are an experimental artifact due to the 0.5° incident beam divergence and the resulting electric noise in the line detector near the intense substrate reflections. A θ-2θ scan from a layer with $x = 0.85$ (not shown) exhibits no detectable peaks from the alloy film, indicating a continued decrease in crystalline quality and suggesting a transition to a nanocrystalline wurtzite structure, consistent with the reported limit for the Al content of $x = 0.6$–0.75 in the rocksalt phase $Cr_{1-x}Al_xN$ solid solution [19,20,23–29].

Figure 2(b) shows a typical XRD ω-rocking curve for the 002 reflection from the $Cr_{0.89}Al_{0.11}N$ layer, obtained using a constant $2\theta = 43.28°$. It has a full width at half maximum of 0.24°, indicating strong crystalline alignment of the (001) planes with the substrate surface. With the addition of Al, the width of the rocking curve increases from 0.27° for pure CrN to 0.49°, 0.43°, and 0.69° for $x = 0.39$, 0.46, and 0.62, respectively, indicating good crystalline alignment for all layers with $x \leqslant 0.62$ but a decreasing crystalline quality with increasing x. This is consistent with the decreasing peak intensity shown in Fig. 2(a) and is similar to what has been reported in previous compositional studies on polycrystalline $Cr_{1-x}Al_xN$ layers [29,38]. The rocking-curve measurement on the $Cr_{0.25}Al_{0.75}N$ layer did not yield a detectable peak, which is attributed to the lower-intensity parallel beam configuration in combination with a low crystalline quality and local strain variations associated with this composition being near the experimental rocksalt to wurtzite stability limit of $x = 0.6$–0.75 [19,23–29].

Figure 2(c) shows a representative high-resolution XRD reciprocal-space map acquired about the asymmetric 113 reflection from a $Cr_{0.89}Al_{0.11}N(001)/MgO(001)$ layer. The color-filled isointensity contour map with a logarithmic scale is plotted in k space, where $k_\perp = 2\sin\theta\cos(\omega - \theta)/\lambda$ and $k_\parallel = 2\sin\theta\sin(\omega - \theta)/\lambda$ correspond to directions perpendicular and parallel to the substrate surface along the perpendicular [001] and [110] directions, respectively. The strong peak due
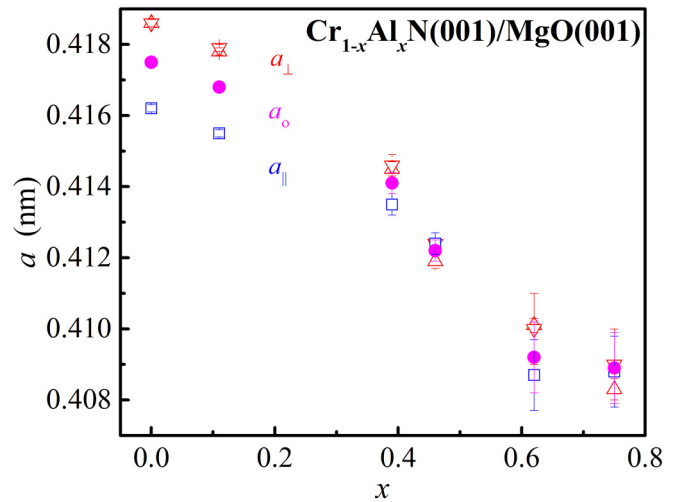

FIG. 3. Out-of-plane $a_\perp$, in-plane $a_\parallel$, and relaxed a_o lattice constants obtained from RSMs (red down triangles, blue squares, magenta circles) and $a_\perp$ obtained from θ-2θ scans (red up triangles) vs Al content x in $Cr_{1-x}Al_xN(001)$ layers grown on MgO(001).

to the MgO 113 reflection has an intensity of 548 counts per s and a full width at half-maximum of $\Delta k_\perp = 0.007$ nm^{-1} and $\Delta k_\parallel = 0.002$ nm^{-1}. The 113 peak from the layer is 97 times less intense and its widths $\Delta k_\perp = 0.019$ nm^{-1} and $\Delta k_\parallel = 0.028$ nm^{-1} are 3 and 14 times larger, respectively. They are in good agreement with the widths $\Delta k_\perp = \Gamma_{2\theta}\cos\theta/\lambda = 0.022$ nm^{-1} and $\Delta k_\parallel = 2\Gamma_\omega\sin\theta/\lambda = 0.020$ nm^{-1} from the peak widths $\Gamma_{2\theta}$ and Γ_ω from the symmetric θ-2θ and 002 rocking-curve scans in Figs. 2(a) and 2(b), respectively. The $Cr_{0.89}Al_{0.11}N$ 113 peak is shifted by 0.046 and 0.056 nm^{-1} from the substrate peak in the parallel and perpendicular directions, respectively, providing values for the in-plane $a_\parallel = 0.4154 \pm 0.0001$ and out of plane $a_\perp = 0.4179 \pm 0.0001$ lattice constants. The smaller $a_\parallel$ value indicates compressive stress, as also evident from the peak position which is below the dotted line in Fig. 2(c) that corresponds to the ω-2θ direction and defines the peak positions for fully relaxed layers. We use the $a_\perp$ and $a_\parallel$ values in combination with an approximate value for the Poisson ratio $\nu = 0.29$ [57], to determine the relaxed lattice constant $a_o = 0.4168 \pm 0.0001$ nm.

Figure 3 is a plot of the in-plane $a_\parallel$, out-of-plane $a_\perp$, and relaxed a_o lattice constants as a function of composition x in $Cr_{1-x}Al_xN(001)$ layers, as determined from reciprocal-space maps. In addition, the plot also includes the $a_\perp$ values determined from the θ-2θ scans plotted in Fig. 2(a). The two datasets for out of plane lattice constants match well, with a maximum deviation of 0.26%. Films with $x = 0$ and 0.11 exhibit a small compressive strain $\varepsilon_\parallel = -0.31$ and -0.33%, respectively, which we attribute to differential thermal contraction during cooling from the deposition temperature of 750 °C to room temperature. We use the reported thermal expansion coefficients for CrN and MgO of 6×10^{-6}K^{-1} [58] and 1.3×10^{-5}K^{-1} [59] to estimate the maximum in-plane compressive strain $\varepsilon_\parallel = -0.5\%$ due to thermal contraction. This strain is larger than for the $x = 0$ and 0.11 samples, indicating that a fraction of the thermal strain is relaxed, resulting in the residual measured strains of -0.31 and -0.33%.
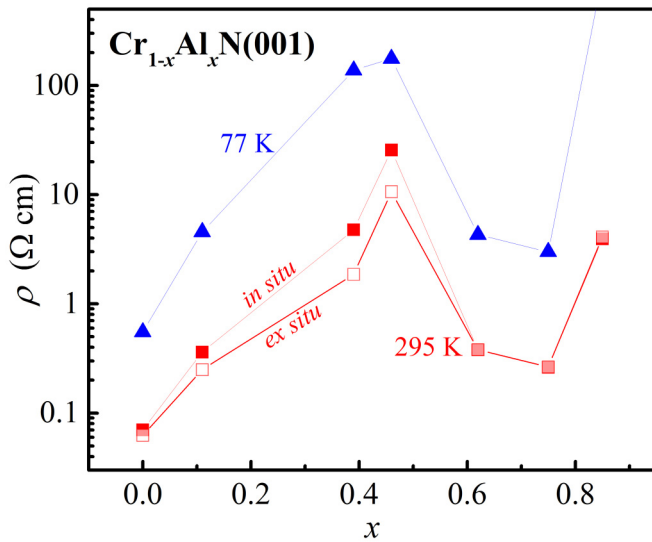
FIG. 4. Electrical resistivity ρ vs x of $Cr_{1-x}Al_xN(001)/MgO(001)$ layers, measured *in situ* and *ex situ* at room temperature (295 K), and in liquid nitrogen at 77 K.

In contrast, all layers with $x \geqslant 0.39$ have $a_{||}$ and $a_{\perp}$ values that are identical within experimental uncertainty, indicating complete strain relaxation which may be attributed to a larger misfit dislocation density which facilitates relaxation through threading dislocation glide during cooling. The relaxed lattice constant decreases with increasing x from $a_o = 0.4175$ nm for pure CrN to $a_o = 0.4089$ nm for $Cr_{0.25}Al_{0.75}N$. Linear extrapolation yields $a_o = 0.407$ nm for AlN in the rocksalt structure, in agreement with the reported values of $a = 4.05$ Å from high-pressure synthesis [60] and 4.07 Å from first-principles calculations [20,61]. The decreasing lattice constant with increasing Al content is also in agreement with previously reported trends for the $Cr_{1-x}Al_xN$ alloy system [19,25,28,29,38].

B. Electronic and optical properties

Figure 4 is a plot of the electrical resistivity versus Al content x in $Cr_{1-x}Al_xN(001)$ layers measured both *in situ* and *ex situ* at room temperature (295 K) as well as *ex situ* in liquid nitrogen at 77 K. The room-temperature resistivity of the CrN(001) layer measured *in situ* and *ex situ* is 0.070 and 0.062 Ω cm, respectively, which is within the previously reported range of 8.2×10^{-3}–$1.7 \times 10^{-1}\Omega$ cm for epitaxial CrN films [1,2,7,8,13,54,56,62,63]. The 11% decrease in the CrN(001) resistivity upon air exposure corresponds to an increase in the measured sheet conductance $\Delta G_s = 0.60 \times 10^{-4}[\Omega/\square]^{-1}$ and is attributed to the formation of a conductive oxynitride layer at the film surface, as has been previously reported based on controlled oxygen exposure studies that found a surface oxynitride layer with a $G_s = 5.9 \times 10^{-5}[\Omega/\square]^{-1}$ [64]. The CrN resistivity at 77 K is 0.55 Ω cm, which is within the previously reported range of 1×10^{-2}–$5\,\Omega$ cm [1,8,13,38,62] and is 9 times larger than the room-temperature value, indicating a negative TCR which is consistent with previous studies on CrN [1,7,38,54,62] and is attributed to electron transport by variable range hopping [1,54]. We note that

carrier localization in CrN [1,7] is attributed to the Mott-Hubbard interaction which splits the filled and empty d_{t2g} bands below the valence-band maximum and above the conduction-band minimum, respectively, resulting in a *p*-to-*d* charge-transfer band gap [2]. In contrast, localization in other transition-metal nitrides has been attributed to (1) complete charge depletion in the *d* bands causing a gap between hybridized *p* and *d* bands like for ScN [65], $Sc_{1-x}Al_xN$ [66], and $Ti_{1-x}Mg_xN$ [67], and (2) weak Anderson localization due to random arrangement of nitrogen vacancies in TaN_x [68,69], NbN_x [70], and HfN_x [71], or random cation site occupation in $Sc_{1-x}Ti_xN$ [72] and $Ti_{1-x}W_xN$ [73]. The data in Fig. 4 show that the *in situ* measured resistivity of $Cr_{1-x}Al_xN(001)$ layers increases by over two orders of magnitude to $\rho = 0.36$, 4.8, and 25 Ω cm with increasing $x = 0.11$, 0.39, and 0.46, respectively, indicating an increasing carrier localization with increasing Al content and a correspondingly lower hopping conduction. This is consistent with first-principles calculations that indicate a weakening of the Cr-Cr next-nearest-neighbor hybridization and therefore a localization of the antibonding Cr 3*d* states [74]. Air exposure causes a resistivity reduction in these alloy layers, like for the pure CrN layer, indicating conductive surface oxynitrides with $G_s = 3.7 \times 10^{-5}$, 9.8×10^{-6}, and $1.6 \times 10^{-6}[\Omega/\square]^{-1}$ for $x = 0.11, 0.39$, and 0.46, respectively. These data suggest that the surface oxides become less conductive with increasing Al content, which is attributed to a reduced surface oxidation of Al-containing layers and/or an increasing band gap with an associated reduced ability for oxygen to act as donor.

A further increase in the Al concentration to $x = 0.62$ and 0.75 leads to a drop in the *in situ* room-temperature resistivity to 0.38 and 0.62 Ω cm, respectively, but ρ increases again to 3.93 Ω cm for $x = 0.85$. We attribute the low resistivity for $x = 0.62$ and 0.75 to an increasing density of interband states that form a conductive band, as discussed below. The *in situ* and *ex situ* values for these two layers are identical within the experimental uncertainty of 5%, and indicate that a possible conductive surface oxynitride would have a $G_s < 1.3 \times 10^{-6}[\Omega/\square]^{-1}$. This value is 19% below that for $x = 0.46$, thus continuing the trend of a decreasing conductance of the surface oxide with increasing Al content. Lastly, the high ρ for $Cr_{0.15}Al_{0.85}N$ is attributed to the transition to a nanocrystalline wurtzite structure which exhibits stronger carrier localization. This is also evident from the high ρ at 77 K, which was too high to be measured with our experimental setup and is therefore estimated to be $>10^3\,\Omega$ cm. In contrast, all other layers exhibit a resistivity at 77 K that is approximately an order of magnitude above the room-temperature value. This is in agreement with previous studies on binary CrN [1] and indicates a Mott temperature $T_M \sim 10^5$ K that is independent of $x \leqslant 0.75$, suggesting that the decreasing localization length is compensated by an increasing density of states at the Fermi level E_f. The reason for the latter is not evident, but may be due to E_f approaching the valence-band top as the energy of filled *d* states increases, caused by a decrease in the Cr-Cr nearest-neighbor hybridization with increasing x [74].

Figure 5(a) shows typical transmittance T and reflectance R spectra from a $Cr_{0.54}Al_{0.46}N$ layer plotted versus photon energy $h\nu = 0.37$–4.5 eV. Interference fringes are evident in both spectra. They are due to reflections from the air-film and
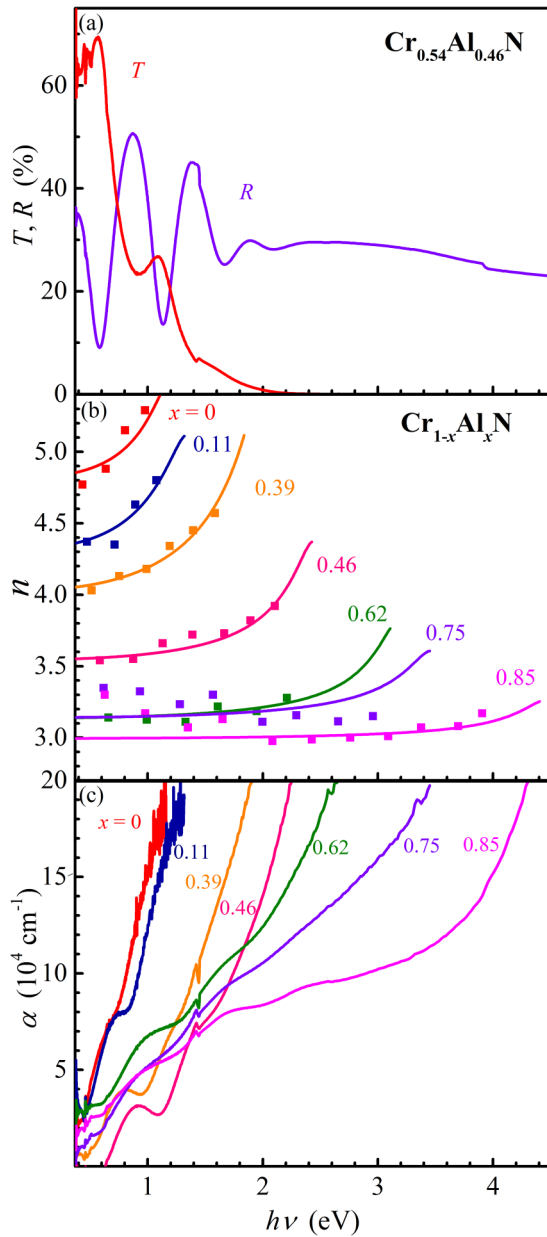
FIG. 5. (a) Representative optical transmittance T and reflectance R spectra from a $Cr_{0.54}Al_{0.46}N(001)$ layer, (b) index of refraction n and (c) absorption coefficient α vs photon energy $h\nu$ for $Cr_{1-x}Al_xN$ with $x = 0$–0.85.

film-substrate interfaces as the minima in R align with the maxima in T and vice versa. In addition, T decreases with increasing $h\nu$, indicating an onset of strong absorption which also leads to the damping of the interference fringes with increasing $h\nu$. The positions of the interference fringe maxima and minima in the reflection spectra are used to determine the index of refraction n in the transparent frequency range, as described in more detail in Sec. II. The resulting n vs photon energy is plotted in Fig. 5(b) for multiple $Cr_{1-x}Al_xN(001)$ layers with $x = 0$–0.85, as labeled. Each data point corresponds to a specific fringe maximum or minimum and the lines are obtained by data fitting using a Lorentz oscillator such that the complex dielectric function $\varepsilon(\omega) = \varepsilon_1 + i\varepsilon_2 =$

$(\varepsilon_o - \varepsilon_\infty)\omega_o{}^2/(\omega_o{}^2 - \omega^2 - i\gamma\omega) = n^2$ [75], where ε_o and ε_∞ are the static and high-frequency dielectric constants, ω_o the resonance frequency, and γ the damping term. The refractive index from the pure CrN layer ($x = 0$) shows an increase from $n = 4.8$–5.5 for $h\nu = 0.38$–1.16 eV which is attributed to the onset interband transitions. These values are in reasonable agreement with the previously reported $n = 5.2$ for CrN for $h\nu = 0.2$–1.0 eV, followed by an increase to a maximum of $n = 5.7$ at $h\nu = 1.48$ [8]. The refractive index decreases with increasing Al content. For example for $h\nu = 0.5$ eV, n decreases to 4.4, 4.1, 3.6, 3.1, 3.1, and 3.0, for $x = 0.11$, 0.39, 0.46, 0.62, 0.75, and 0.85, respectively. In addition, the dispersion $dn/d\nu$ decreases with increasing x while the onset for the steep increase in n shifts to larger photon energies. The decreasing refractive index with increasing x is consistent with a predicted $n = 2$ for rocksalt AlN over a large photon energy range $h\nu = 0$–5 eV [46].

Figure 5(c) is a plot of the optical absorption coefficient α versus photon energy $h\nu$ for the same $Cr_{1-x}Al_xN$ layers with $x = 0$–0.85. It is determined from the measured optical spectra as described in Sec. II. The absorption coefficient of the pure CrN layer increases steeply from 4.2×10^4 cm^{-1} at $h\nu = 0.50$ eV to 1.5×10^5 cm^{-1} at $h\nu = 1.00$ eV. This increase is attributed to electron transitions from the N $2p$-like valence band to the majority e_g band [2,8]. The $Cr_{1-x}Al_xN$ alloys show similar absorption curves, with the steep absorption increase moving to higher photon energies as the Al content is increased. As a consequence, the photon energy where $\alpha = 1.5 \times 10^5$ cm^{-1} increases to 1.11, 1.68, 2.05, 2.26, 2.86, and 3.98 eV for $x = 0.11$, 0.39, 0.46, 0.62, 0.75, and 0.85, respectively. This indicates a continuously increasing optical band gap with increasing x, as discussed below. In addition, layers with $x = 0.62$, 0.75, and 0.85 show considerable absorption $\alpha = (5$–$10) \times 10^4$ cm^{-1} at $h\nu = 1$–2 eV, that is, at photon energies below the strong onset. As a result, the absorption coefficient at $h\nu = 1$ eV initially decreases continuously from 1.5×10^5 cm^{-1} for CrN to $\alpha = 12 \times 10^4$, 4.0×10^4, and 3.0×10^4 cm^{-1} with increasing $x = 0.11$, 0.39, and 0.46, but then increases to 6.8×10^4, 5.2×10^4, and 5.2×10^4 cm^{-1} for $x = 0.62$, 0.75, and 0.85, respectively. This suggests a non-negligible density of states within the band gap for layers with $x \geqslant 0.62$. These states are expected to form a conductive band and are likely causing the reduced resistivity for $x \geqslant 0.62$ presented in Fig. 4. We note that the oscillations which are most prominent for the $x = 0.39$ and 0.46 curves around 0.9 eV are a residual effect from interference fringes while the discontinuity in the plotted curves at $h\nu = 1.44$ eV is an experimental artifact due to a detector change.

Figure 6 is a plot of the optical band gap E_g of $Cr_{1-x}Al_xN$ as a function of x, determined from the measured absorption coefficient using Tauc plots for direct band gaps [76]. The inset shows a typical Tauc plot for the $Cr_{0.54}Al_{0.46}N$ layer, where the plotted $(\alpha h\nu)^2$ vs $h\nu$ curve exhibits a strong positive curvature at photon energies near the band gap and a linear region which allows extrapolation to the x axis and determination of $E_g = 1.97$ eV as indicated by the black dashed line. We assume parabolic bands for this analysis, based on the reported parabolic bands near the direct gap transitions in the calculated band structures for both rocksalt CrN [2,11] and
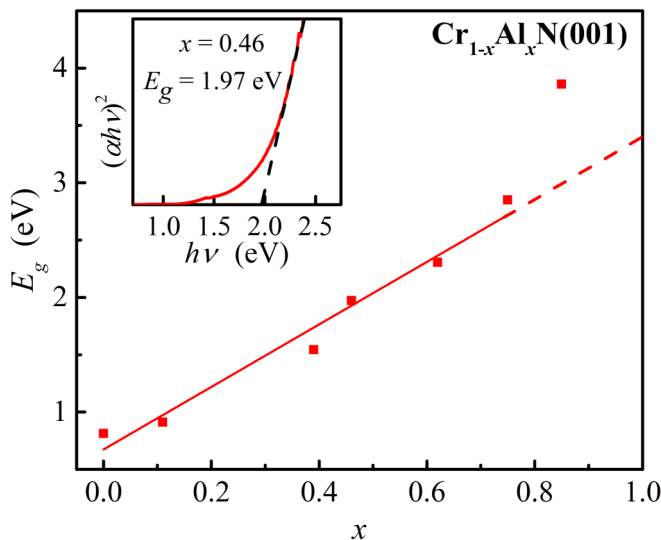
FIG. 6. Optical band gap E_g vs x in $Cr_{1-x}Al_xN$ alloys, determined using Tauc plots as illustrated in the inset for $x = 0.46$.

rocksalt AlN [41–43,45,46]. Similar Tauc plot analyses are done for all samples, as shown in the Supplemental Material to this paper [77], yielding the E_g values plotted in the main figure. The optical gap for CrN ($x = 0$) is 0.81 eV, which is slightly larger than the previously published 0.70 eV [8,13]. This value corresponds to the gap at the Γ point between the N-2p-like valence band and the majority spin e_g conduction band [2,8]. However, CrN also has a smaller indirect gap of 0.2 eV [2,8,12].

The plotted optical band gap increases continuously with increasing x, following approximately a linear trend for $x \leqslant 0.75$. This is indicated by the plotted line through the data points which is the result from curve fitting and corresponds to $E_g(x) = 0.64 + 2.81x$. Extrapolating this expression to $x = 1$ suggests an optical band gap for cubic rocksalt AlN of 3.45 eV. This is smaller than what has been previously predicted for the direct gap in cubic rocksalt AlN of $E_g = 5.0$–6.9 [41–44]. Similar to CrN, rocksalt structure AlN is predicted to have a slightly smaller indirect gap of $E_g = 4.0$–5.0 [41–47]. Therefore, $Cr_{1-x}Al_xN$ alloys in the rocksalt structure are expected to have an indirect gap that is smaller than the direct transition detected by our optical measurements and plotted in Fig. 6. However, we note that the symmetry breaking due to the random occupation of cation sites by Cr and Al atoms may make all interband transitions optically active, such that the plotted gap energies may be more reflective of the fundamental indirect gap in $Cr_{1-x}Al_xN$ alloys than the larger direct transition. This may also explain the relatively small extrapolated E_g for cubic rocksalt AlN.

The measured E_g for the $Cr_{0.15}Al_{0.85}N$ layer is 3.86 eV, which is well above the linear trend for $x < 0.75$. We attribute the steep slope between $x = 0.75$ and 0.85 to a transition to a nanocrystalline microstructure, as discussed above. More specifically, this layer has likely atomic bonding that resembles AlN in the wurtzite structure, resulting in a correspondingly increased band gap, since the gap of AlN in the wurtzite structure of 6.11 eV [22] is 22–53% above the gap for cubic rocksalt AlN [41–47].

IV. CONCLUSIONS

300-nm thick $Cr_{1-x}Al_xN(001)$ films were grown on MgO(001) substrates by ultrahigh-vacuum reactive magnetron cosputtering at 750 °C. Increasing the Al to Cr target power ratio from $P_{Al}/P_{Cr} = 0$ to 7.9 results in films with Al content $x = 0$–0.85 and a constant cation to anion ratio of 1.00 ± 0.05, as confirmed by RBS. X-ray diffraction indicates a rocksalt solid solution for $x \leqslant 0.75$ with in-plane and out-of-plane lattice constants decreasing from $a_\perp = 0.4186$ nm and $a_\parallel = 0.4160$ nm for pure CrN to $a_\perp = a_\parallel = 0.4083$ nm for $Cr_{0.25}Al_{0.75}N$. The room-temperature resistivity increases with Al content from $0.070\,\Omega$ cm for $x = 0$ to $26\,\Omega$ cm for $x = 0.46$ which may be attributed to an increasing carrier localization associated with a decreasing Cr-Cr nearest-neighbor hybridization. However, ρ decreases again to $<0.38\,\Omega$ cm as x is increased further to $\geqslant 0.62$. This is attributed to conduction by states in the band gap which also lead to considerable subgap absorption observed for samples with $x \geqslant 0.62$. The resistivity increases upon cooling to 77 K by approximately one order of magnitude for all layers with $x \leqslant 0.75$, suggesting that the decreasing localization length is compensated by an increasing density of states at the Fermi level. Optical transmission and reflection measurements are used to determine the optical band gap, which increases from $E_g = 0.81$ eV for $x = 0$ to $E_g = 2.85$ eV for $x = 0.75$. The refractive index below the gap (at $h\nu = 0.5$ eV) continuously decreases with increasing x from $n = 4.8$ for CrN to $n = 3.1$ for $Cr_{0.15}Al_{0.85}N$. This work demonstrates that $Cr_{1-x}Al_xN$ alloys in the rocksalt phase retain the semiconducting properties of the cubic parent nitrides CrN and AlN in the rocksalt structure, indicating the potential use for optoelectronic, magnetoelectric, or thermoelectric applications.

ACKNOWLEDGMENT

[1] X. Y. Zhang, J. S. Chawla, B. M. Howe, and D. Gall, Phys. Rev. B **83**, 165205 (2011).

[2] A. Herwadkar and W. R. L. Lambrecht, Phys. Rev. B **79**, 035125 (2009).

[3] P. A. Bhobe, A. Chainani, M. Taguchi, T. Takeuchi, R. Eguchi, M. Matsunami, K. Ishizaka, Y. Takata, M. Oura, Y. Senba, H. Ohashi, Y. Nishino, M. Yabashi, K. Tamasaku, T. Ishikawa, K. Takenaka, H. Takagi, and S. Shin, Phys. Rev. Lett. **104**, 236404 (2010).

[4] T. Cheiwchanchamnangij and W. R. L. Lambrecht, Phys. Rev. B **101**, 085103 (2020).

[5] J. Ebad-Allah, B. Kugelmann, F. Rivadulla, and C. A. Kuntscher, Phys. Rev. B **94**, 195118 (2016).

[6] B. Alling, T. Marten, and I. A. Abrikosov, Phys. Rev. B **82**, 184430 (2010).

[7] X. Y. Zhang, J. S. Chawla, R. P. Deng, and D. Gall, Phys. Rev. B **84**, 073101 (2011).

[8] X. Y. Zhang and D. Gall, Phys. Rev. B **82**, 045116 (2010).

[9] A. Ney, R. Rajaram, S. S. P. Parkin, T. Kammermeier, and S. Dhar, Appl. Phys. Lett. **89**, 112504 (2006).

[10] K. Alam, S. M. Disseler, W. D. Ratcliff, J. A. Borchers, R. Ponce-Pérez, G. H. Cocoletzi, N. Takeuchi, A. Foley, A. Richard, D. C. Ingram, and A. R. Smith, Phys. Rev. B **96**, 104433 (2017).

[11] A. S. Botana, F. Tran, V. Pardo, D. Baldomir, and P. Blaha, Phys. Rev. B **85**, 235118 (2012).

[12] A. S. Botana, V. Pardo, D. Baldomir, and P. Blaha, Phys. Rev. B **87**, 075114 (2013).

[13] D. Gall, C.-S. Shin, R. T. Haasch, I. Petrov, and J. E. Greene, J. Appl. Phys. **91**, 5882 (2002).

[14] Y. C. Chim, X. Z. Ding, X. T. Zeng, and S. Zhang, Thin Solid Films **517**, 4845 (2009).

[15] H. C. Barshilia, N. Selvakumar, B. Deepthi, and K. S. Rajam, Surf. Coat. Technol. **201**, 2193 (2006).

[16] A. Y. Polyakov, N. B. Smirnov, A. V. Govorkov, R. M. Frazier, J. Y. Liefer, G. T. Thaler, C. R. Abernathy, S. J. Pearton, and J. M. Zavada, Appl. Phys. Lett. **85**, 4067 (2004).

[17] S. G. Yang, A. B. Pakhomov, S. T. Hung, and C. Y. Wong, Appl. Phys. Lett. **81**, 2418 (2002).

[18] P. Eklund, S. Kerdsongpanya, and B. Alling, J. Mater. Chem. C **4**, 3905 (2016).

[19] A. Sugishima, H. Kajioka, and Y. Makino, Surf. Coat. Technol. **97**, 590 (1997).

[20] R. F. Zhang and S. Veprek, Acta Mater. **55**, 4615 (2007).

[21] D. Holec, F. Rovere, P. H. Mayrhofer, and P.B. Barna, Scr. Mater. **62**, 349 (2010).

[22] L. Zhou, D. Holec, and P. H. Mayrhofer, J. Appl. Phys. **113**, 43511 (2013).

[23] M. Kawate, A. K. Hashimoto, and T. Suzuki, Surf. Coat. Technol. **165**, 163 (2003).

[24] A. Kimura, M. Kawate, H. Hasegawa, and T. Suzuki, Surf. Coat. Technol. **169–170**, 367 (2003).

[25] Y. Makino and K. Nogi, Surf. Coat. Technol. **98**, 1008 (1998).

[26] H. Willmann, P. H. Mayrhofer, P. O. Persson, A. E. Reiter, L. Hultman, and C. Mitterer, Scr. Mater. **54**, 1847 (2006).

[27] A. E. Reiter, V. H. Derflinger, B. Hanselmann, T. Bachmann, and B. Sartory, Surf. Coat. Technol. **200**, 2114 (2005).

[28] M. Hirai, Y. Ueno, T. Suzuki, W. Jiang, C. Grigoriu, and K. Yatsui, Jpn. J. Appl. Phys. **40**, 1056 (2001).

[29] O. Banakh, P. E. Schmid, R. Sanjinés, and F. Lévy, Surf. Coat. Technol. **163–164**, 57 (2003).

[30] O. Knotek, F. Löffler, and H. J. Scholl, Surf. Coat. Technol. **45**, 53 (1991).

[31] H. Hasegawa, M. Kawate, and T. Suzuki, Surf. Coat. Technol. **200**, 2409 (2005).

[32] E. Lugscheider, K. Bobzin, S. Bärwulf, and T. Hornig, Surf. Coat. Technol. **133–134**, 540 (2000).

[33] B.C. Schramm, H. Scheerer, H. Hoche, E. Broszeit, E. Abele, and C. Berger, Surf. Coat. Technol. **188–189**, 623 (2004).

[34] F. Rovere, D. Music, S. Ershov, M. T. Baben, H. G. Fuss, P. H. Mayrhofer, and J. M. Schneider, J. Phys. D: Appl. Phys. **43**, 35302 (2010).

[35] B. Alling, L. Hultberg, L. Hultman, and I. A. Abrikosov, Appl. Phys. Lett. **102**, 031910 (2013).

[36] P. H. Mayrhofer, A. Hörling, L. Karlsson, J. Sjölén, T. Larsson, C. Mitterer, and L. Hultman, Appl. Phys. Lett. **83**, 2049 (2003).

[37] A. le Febvrier, N. Van Nong, G. Abadias, and P. Eklund, Appl. Phys. Express **11**, 051003 (2018).

[38] R. Sanjinés, O. Banakh, C. Rojas, P. Schmid, and F. Lévy, Thin Solid Films **420–421**, 312 (2002).

[39] H. Willmann, M. Beckers, J. Birch, P. H. Mayrhofer, C. Mitterer, and L. Hultman, Thin Solid Films **517**, 598 (2008).

[40] H. Willmann, M. Beckers, F. Giuliani, J. Birch, P. H. Mayrhofer, C. Mitterer, and L. Hultman, Scr. Mater. **57**, 1089 (2007).

[41] Z. Y. Jiao, S. H. Ma, and J. F. Yang, Solid State Sci. **13**, 331 (2011).

[42] X. Zhang, Z. Chen, S. Zhang, R. Liu, H. Zong, Q. Jing, G. Li, M. Ma, and W. Wang, J. Phys.: Condens. Matter **19**, 425231 (2007).

[43] N. E. Christensen and I. Gorczyca, Phys. Rev. B **50**, 4397 (1994).

[44] P. E. Van Camp, V. E. Van Doren, and J. T. Devreese, Phys. Rev. B **44**, 9056 (1991).

[45] W. Feng, S. Cui, H. Hu, W. Zhao, and Z. Gong, Physica B **405**, 555 (2010).

[46] Y. C. Cheng, X. L. Wu, J. Zhu, L.L. Xu, S. H. Li, and P. K. Chu, J. Appl. Phys. **103**, 73707 (2008).

[47] H. Berkok, A. Tebboune, A. Saim, and A. H. Belbachir, Physica B **411**, 1 (2013).

[48] J. Li, K. B. Nam, M. L. Nakarmi, J. Y. Lin, H. X. Jiang, P. Carrier, and S.-H. Wei, Appl. Phys. Lett **83**, 5163 (2003).

[49] J. S. Chawla, F. Zahid, H. Guo, and D. Gall, Appl. Phys. Lett **97**, 132106 (2010).

[50] P. Y. Zheng, R. P. Deng, and D. Gall, Appl. Phys. Lett **105**, 131603 (2014).

[51] O. S. Heavens, *Optical Properties of Thin Solid Films* (Dover, New York, 1991).

[52] J. Lin, J. J. Moore, B. Mishra, M. Pinkas, X. Zhang, and W. D. Sproul, Thin Solid Films **517**, 5798 (2009).

[53] J. Lin, B. Mishra, J. J. Moore, and W. D. Sproul, Surf. Coat. Technol. **201**, 4329 (2006).

[54] D. Gall, C.-S. Shin, T. Spila, M. Odén, M. J. H. Senna, J. E. Greene, and I. Petrov, J. Appl. Phys. **91**, 3589 (2002).

[55] K. Balasubramanian, S. V. Khare, and D. Gall, Acta Mater. **159**, 77 (2018).

[56] C. Constantin, M. B. Haider, D. Ingram, and A. R. Smith, Appl. Phys. Lett. **85**, 6371 (2004).

[57] U. Wiklund, M. Bromark, M. Larsson, P. Hedenqvist, and S. Hogmark, Surf. Coat. Technol. **91**, 57 (1997).

[58] M. Eddine, F. Sayetat, and E. F. Bertait, Acad. Sci. Ser. B **269**, 574 (1969).

[59] H. Landolt and R. Börnstein, *Numerical Data and Functional Relationships in Science and Technology, Group III* (Springer, Berlin, 1975), Vol. 7.

[60] H. Vollstadt, E. Ito, S. iti Akimoto, M. Akaishi, and O. Fukunaga, Proc. Jpn. Acad. Ser. B: Phys. Biol. Sci. **66**, 7 (1990).

[61] A. J. Wang, S. L. Shang, Y. Du, Y. Kong, L. J. Zhang, L. Chen, D. D. Zhao, and Z. K. Liu, Comput. Mater. Sci. **48**, 705 (2010).

[62] P. A. Anderson, R. J. Kinsey, S. M. Durbin, A. Markwitz, V. J. Kennedy, A. Asadov, W. Gao, and R. J. Reeves, J. Appl. Phys. **98**, 043903 (2005).

[63] K. Inumaru, K. Koyama, N. Imo-oka, and S. Yamanaka, Phys. Rev. B **75**, 054416 (2007).

[64] M. E. McGahay and D. Gall, Appl. Phys. Lett. **114**, 131602 (2019).

[65] R. Deng, B. D. Ozsdolay, P. Y. Zheng, S. V Khare, and D. Gall, Phys. Rev. B **91**, 045104 (2015).

[66] R. Deng, P. Y. Zheng, and D. Gall, J. Appl. Phys. **118**, 015706 (2015).

[67] B. Wang, S. Kerdsongpanya, M. E. McGahay, E. Milosevic, P. Patsalas, and D. Gall, J. Vac. Sci. Technol. A **36**, 061501 (2018).

[68] C.-S. Shin, D. Gall, P. Desjardins, A. Vailionis, H. Kim, I. Petrov, J. E. Greene, and M. Odén, Appl. Phys. Lett. **75**, 3808 (1999).

[69] C.-S. Shin, D. Gall, Y.-W. Kim, P. Desjardins, I. Petrov, J.E. Greene, M. Odén, and L. Hultman, J. Appl. Phys. **90**, 2879 (2001).

[70] K. Zhang, K. Balasubramanian, B. D. Ozsdolay, C. P. Mulligan, S. V. Khare, W. T. Zheng, and D. Gall, Surf. Coat. Technol. **288**, 105 (2016).

[71] H.-S. Seo, T.-Y. Lee, I. Petrov, J. E. Greene, and D. Gall, J. Appl. Phys. **97**, 083521 (2005).

[72] D. Gall, I. Petrov, and J. E. Greene, J. Appl. Phys. **89**, 401 (2001).

[73] F. Tian, J. D'Arcy-Gall, T.-Y. Lee, M. Sardela, D. Gall, I. Petrov, and J. E. Greene, J. Vac. Sci. Technol. A **21**, 140 (2003).

[74] B. Alling, T. Marten, I. A. Abrikosov, and A. Karimi, J. Appl. Phys. **102**, 44314 (2007).

[75] M. Born and K. Huang, *Dynamical Theory of Crystal Lattices* (Oxford University Press, London, 1954).

[76] J. Tauc, R. Grigorovici, and A. Vancu, Phys. Status Solidi **15**, 627 (1966).

[77] See Supplemental Material at http://link.aps.org/supplemental/10.1103/PhysRevB.101.205206 for the Tauc plots of all samples in this study.